

Metric 3D Reconstruction and Texture Acquisition of Surfaces of Revolution from a Single Uncalibrated View

Carlo Colombo, Alberto Del Bimbo, and Federico Pernici

Abstract—Image analysis and computer vision can be effectively employed to recover the three-dimensional structure of imaged objects, together with their surface properties. In this paper, we address the problem of metric reconstruction and texture acquisition from a single uncalibrated view of a surface of revolution (SOR). Geometric constraints induced in the image by the symmetry properties of the SOR structure are exploited to perform self-calibration of a natural camera, 3D metric reconstruction, and texture acquisition. By exploiting the analogy with the geometry of single axis motion, we demonstrate that the imaged apparent contour and the visible segments of two imaged cross sections in a single SOR view provide enough information for these tasks. Original contributions of the paper are: single view self-calibration and reconstruction based on planar rectification, previously developed for planar surfaces, has been extended to deal also with the SOR class of curved surfaces; self-calibration is obtained by estimating both camera focal length (one parameter) and principal point (two parameters) from three independent linear constraints for the SOR fixed entities; the invariant-based description of the SOR scaling function has been extended from affine to perspective projection. The solution proposed exploits both the geometric and topological properties of the transformation that relates the apparent contour to the SOR scaling function. Therefore, with this method, a metric localization of the SOR occluded parts can be made, so as to cope with them correctly. For the reconstruction of textured SORs, texture acquisition is performed without requiring the estimation of external camera calibration parameters, but only using internal camera parameters obtained from self-calibration.

Index Terms—Surface of revolution, camera self-calibration, single-view 3D metric reconstruction, texture acquisition, projective geometry, image-based modeling.

1 INTRODUCTION

IN the last few years, the growing demand for realistic three-dimensional (3D) object models for graphic rendering, creation of nonconventional digital libraries, and population of virtual environments has renewed the interest in the reconstruction of the geometry of 3D objects and in the acquisition of their textures from one or more camera images. In fact, solutions based on image analysis can be efficiently employed in all those cases in which 1) the original object is not available and only its photographic reproduction can be used, or 2) the physical properties of the surface of the object make its acquisition difficult, or even impossible through structured light methods, or 3) the object's size is too large for other automatic acquisition methods.

In this paper, we address the task of metric reconstruction and texture acquisition from a single uncalibrated image of an SOR. We follow a method which exploits geometric constraints of the imaged object assuming a camera with zero skew and known aspect ratio. The geometric constraints for camera self-calibration and object reconstruction are derived from the symmetry properties of the imaged SOR structure. The key idea is that, since an SOR is a nontrivial "repeated structure" generated by the rotation of a planar curve around an axis, it can, in principle, be recovered by properly

extending and combining together single image planar scene reconstruction and single axis motion constraints.

In the following, we summarize recent contributions on 3D object reconstruction (Section 1.1); we discuss then new research results on surfaces of revolution and, more generally, on straight uniform generalized cylinders (Section 1.2) and, finally, provide an outline of the rest of the paper and a list of the principal contributions (Section 1.3).

1.1 Three-Dimensional Object Reconstruction Using Prior Knowledge

Solutions for the reconstruction of the geometry of 3D objects from image data include classic triangulation [19], [13], visual hulls [47], [42], dense stereo [40], and level sets methods [12] (see [44] for a recent survey). An essential point for metric reconstruction of 3D objects is the availability of internal camera parameters. In particular, self-calibration of the camera [35] is important in that, although less accurate than offline calibration [4], [18], it is the only possible solution when no direct measurements can be made in the scene, as, for example, in applications dealing with archive photographs and recorded video sequences. Effective camera self-calibration and object reconstruction can be obtained by exploiting prior knowledge about the scene, encoded in the form of constraints on either scene geometry or motion.

Most of the recent research contributions employ constraints on scene geometry. The presence of a "repeated structure" [32] is a classical example of geometric constraint frequently used. This happens because the image of a repeated structure is tantamount to multiple views of the same structure. In real applications, this can have to do with

• The authors are with Dipartimento di Sistemi e Informatica-Università di Firenze, Via Santa Maria 3, I-50139 Firenze, Italy.
E-mail: {colombo, delbimbo, pernici}@dsi.unifi.it.

Manuscript received 31 July 2003; revised 9 Feb. 2004; accepted 26 Apr. 2004.
Recommended for acceptance by D. Forsyth.
For information on obtaining reprints of this article, please send e-mail to: tpami@computer.org, and reference IEEECS Log Number TPAMI-0203-0703.

planes, lines, etc., occurring in particular (e.g., parallel, orthogonal) spatial arrangements. In a repeated structure, the epipolar geometry induced in the image by multiple instances of the same object can be expressed through projective homologies which require less parameters and, therefore, are more robust to estimate [50]. A further advantage of geometrically constrained reconstruction is that fewer (and, in special cases, just one) images are required. An interactive model-based approach, working with stereo or single images, has been proposed by Debevec et al. in [10], where the scene is represented as a constrained hierarchical model of parametric polyhedral primitives—such as boxes, prisms—called blocks. The user can constrain the sizes and positions of any block in order to simplify the reconstruction problem. All these constraints are set in the 3D space, thus requiring a complex nonlinear optimization to estimate camera positions and model parameters. Liebowitz et al. have suggested to perform calibration from scene constraints by exploiting orthogonality conditions, in order to reconstruct piecewise planar architectural scenes [29], [28]. Single view piecewise planar reconstruction and texture acquisition has also been addressed by Sturm and Maybank following a similar approach [46], [45].

Motion constraints for self-calibration and reconstruction have been derived mainly for the case of scenes undergoing planar motion [3]. In particular, recent works have exploited single axis motion to reconstruct objects of any shape that rotate on a turntable [15], [9], [24], [31]. Apart from algorithmic differences in the reconstruction phase, motion fixed entities (e.g., the imaged axis of rotation and the vanishing line of the plane of rotation) are first estimated from the image sequence and then used to calibrate the camera. However, these turntable approaches do not succeed to perform a complete camera self-calibration. As a consequence of this, reconstruction is affected by a 1D projective ambiguity along the rotation axis.

In the case of textured 3D objects, the texture must be acquired from the image in order to backproject correctly image data onto the reconstructed object surface. Generally speaking, for the case of curved objects, no geometric constraints can be set and texture acquisition requires the estimation of the external calibration parameters (camera position and orientation). There are basically two methods for estimating external calibration from image data and a known 3D structure. The first method exploits the correspondence between selected points on the 3D object and their images [37], [6]. The second method works directly on the image plane and minimizes the mismatch between the original object silhouette and the synthetic silhouette obtained by projecting the 3D object onto the image [22], [33].

For planar objects, texture acquisition using surface geometric constraints has been solved by Liebowitz et al. in [28], without requiring the explicit computation of external camera parameters; projective distortions are rectified so as to represent textures as rectangular images. Sturm and Maybank, in [46], have also performed texture acquisition from planar surfaces, omitting the rectification step; this saves computation time but requires larger memory space to store the textures.

1.2 Straight Homogeneous Generalized Cylinders and Surfaces of Revolution

Surfaces of Revolution (SORs) represent a class of surfaces that are generated by rotating a planar curve (scaling function) around an axis. They are very common in

man-made objects and, thus, of great relevance for a large number of applications. SORs are a subclass of Straight Homogeneous Generalized Cylinders (SHGCs). SHGCs have been extensively studied under different aspects: description, grouping, recognition, recovery, and qualitative surface reconstruction (for an extensive review, see [1]). Their invariant properties and use have been investigated by several authors. Ponce et al. [36] have proposed invariant properties of SHGC imaged contours that have been exploited for description and recovery by other researchers [26], [38], [30], [39], [48], [57], [56]. Abdallah and Zisserman [2] have instead defined invariant properties of the SOR scaling function under affine viewing conditions, thus allowing recognition of objects of the same class from a single view. However, they have left to future work the problem of finding the analogous invariants in the perspective view case, and solving the problem of 3D metric reconstruction of SORs.

Reconstruction of a generic SHGC from a single view, either orthographic or perspective, is known to be an under-constrained problem, except for the case of SORs [17]. Utcke and Zisserman [49] have recently used two imaged cross sections to perform projective reconstruction (up to a 2 DOF transformation) of SORs from a single uncalibrated image. Contributions addressing the problem of metric reconstruction of SORs from a single perspective view may also be found [54], [8]. Wong et al. in [54] have addressed reconstruction of SOR structure from its silhouette given a single uncalibrated image; calibration is obtained following the method described in [53], [55]. However, with this method, only the focal length can be estimated from a single view, with the assumptions of zero skew and principal point being at the image center. The reconstruction is affected by a 1-parameter ambiguity: Although this can be fixed by localizing an imaged cross section of the surface, one of the major problems in this approach is that the silhouette is related directly to its generating contour on the surface. This is an incorrect assumption that makes it impossible to capture the correct object geometry in the presence of self-occlusions, as shown in [11]. Single view metric reconstruction of SORs was also addressed by Colombo et al. who have discussed in [8] the basic ideas underlying the approach presented in this paper.

Texture acquisition of straight uniform generalized cylinders (SUGCs), which are a special subclass of SORs, has been addressed by Pitas et al. [34]. In this approach, texture is obtained as a mosaic image gathering visual information from several images. Since texture is not metrically sampled, the quality of the global visual appearance of the object is affected in some way.

1.3 Paper Organization and Main Contribution

The paper is organized as follows: Section 2 provides background material on basic geometric properties of SORs and states the analogy between single axis motion and surfaces of revolution. Section 3 describes in detail the solutions proposed, specifically addressing computation of the fixed entities, camera calibration, reconstruction of 3D structure, and texture acquisition. Metric reconstruction of the 3D structure of the SOR is reformulated as the problem of determining the shape of a meridian curve. The inputs to the algorithms are the visible segments of two elliptical imaged SOR cross sections and the silhouette of the object apparent contour. Camera self-calibration is obtained by deriving three independent linear constraints from the fixed entities in a single view of an SOR. Texture acquisition is obtained by

exploiting the special properties of an SOR's structure. In fact, texture is not acquired through the estimation of external calibration parameters, but is obtained directly from the image, by using the same parameters that have been computed for the 3D SOR reconstruction: this avoids errors due to additional computations. Self-calibration information is exploited in the resampling phase.

The main contributions of the paper with reference to the recent literature can be summarized as follows:

1. Single-view reconstruction based on planar rectification, originally introduced in [28] for planar surfaces, has been extended to deal also with the SOR class of curved surfaces.
2. Self-calibration of a natural camera (3 dofs) is obtained from a single image of an SOR. This improves the approach presented in [55], in which the calibration of a natural camera requires the presence of two different SORs in the same view. Moreover, since self-calibration is based on two visible elliptical segments, it can also be used to calibrate turntable sequences and remove the 1D projective reconstruction ambiguity due to under-constrained calibration experienced so far in the literature of motion-constrained reconstruction [23].
3. The invariant-based description of the SOR scaling function discussed in [2] is extended from affine to perspective viewing conditions.
4. Since the approach exploits both the geometric and topological properties of the transformation that relates the apparent contour to the scaling function, a metric localization of occluded parts can be performed and the scaling function can be reconstructed piecewise. In this regard, the method improves the SOR reconstruction approach described in [51].
5. Texture acquisition does not require the explicit computation of external camera parameters; therefore, the results developed in [28] and [46] for planar surfaces are extended to the SOR class of curved surfaces. Moreover, since SORs are a superclass of the SUGC class of curved surfaces, texture acquisition extends the solution presented in [34].

In Section 4, experimental results on both synthetic and real data are presented and discussed. Finally, in Section 5 conclusions are drawn and future work is outlined. Mathematical proofs are reported in the Appendices.

2 BACKGROUND

In this section, we review the basic terminology and geometric properties of SORs under perspective projection. We also discuss an important analogy between properties as derived from a single SOR image and those of a sequence of images obtained from single axis motion: this analogy will be exploited in the calibration, reconstruction, and texture acquisition algorithms, discussed in Section 3.

2.1 Basic Terminology

Mathematically, a *surface of revolution* can be thought of as obtained by revolving a planar curve $\rho(z)$, referred to as *scaling function*, around a straight axis z (*symmetry axis*). Therefore, SORs can be parametrized as $\mathbf{P}(\theta, z) = (\rho(z) \cos(\theta), \rho(z) \sin(\theta), z)$, with $\theta \in [0, 2\pi]$, $z \in [0, 1]$. In the 3D space, all *parallels* (i.e., cross sections with planes $z = \text{constant}$) are circles. *Meridians* (i.e., the curves obtained by cutting the SOR with

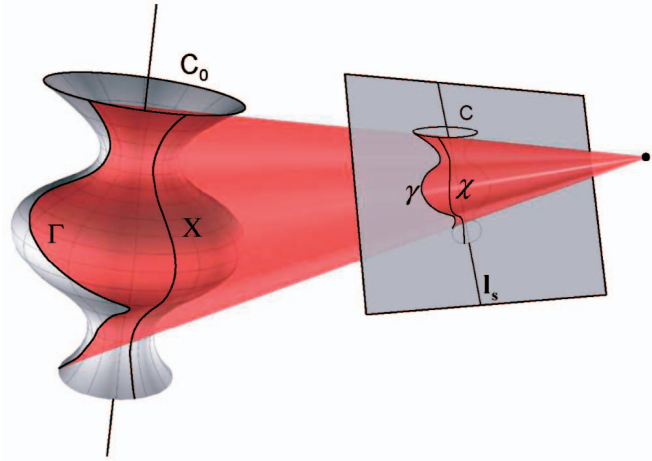


Fig. 1. Imaged SOR geometry. Γ and γ are, respectively, part of the contour generator and of the apparent contour. The translucent cone is the visual hull for the apparent contour. X and χ are, respectively, a meridian and its projection. The ellipse c is the edge corresponding to the parallel C_0 .

planes $\theta = \text{constant}$) all have the same shape, coinciding with that of the SOR scaling function. Locally, parallels and meridians are mutually orthogonal in the 3D space, but not in a 2D view. Two kinds of curves can arise in the projection of an SOR: *limbs* and *edges* [11]. A limb, also referred to as *apparent contour*, is the image of the points at which the surface is smooth and projection rays are tangent to the surface. The corresponding 3D curve is referred to as *contour generator*. An edge is the image of the points at which the surface is not smooth and has discontinuities in the surface normal. Fig. 1 depicts an SOR and its projection. Under general viewing conditions, the contour generator is not a planar curve and is therefore different from a meridian [25]. Depending on this, the apparent contour also differs from the imaged meridian. Parallels always project onto the image as ellipses. Edges are elliptical segments that are the projection of partially or completely visible surface parallels.

2.2 Basic Imaged SOR Properties

Most of the properties of imaged SORs can be expressed in terms of projective transformations called *homologies*. These are special planar transformations that have a line of fixed points (the homology axis) and a fixed point (the vertex) that does not belong to the axis [43]. In homogeneous coordinates, a planar homology is represented by a 3×3 matrix W transforming points as $\mathbf{x}' = W\mathbf{x}$. This matrix has two equal and one distinct real eigenvalues, with eigenspaces, respectively, of dimension two and one. It can be parametrized as

$$W = I + (\mu - 1) \frac{\mathbf{v}\mathbf{l}^T}{\mathbf{v}^T \mathbf{l}}, \quad (1)$$

where I is the 3×3 identity matrix, \mathbf{l} is the axis, \mathbf{v} is the vertex, and μ is the ratio of the distinct eigenvalue to the repeated one. A planar homology has five degrees of freedom (dof); hence, it can be obtained from three point correspondences. In the special case $\mu = -1$, the dofs are reduced to four, and the corresponding homology H is said to be *harmonic*. An imaged SOR satisfies the following two fundamental properties, the geometric meaning of which is illustrated in Fig. 2.

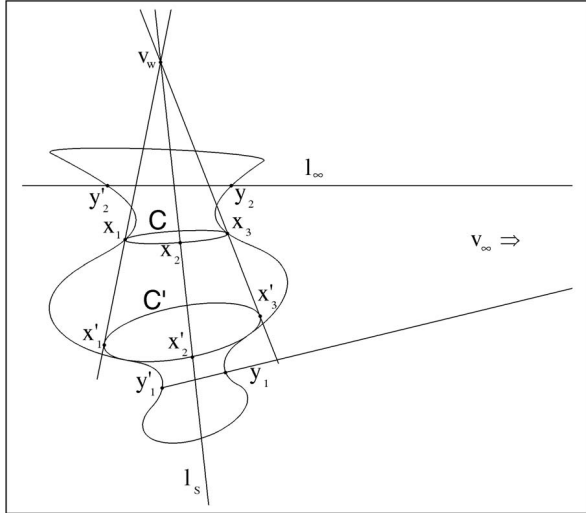


Fig. 2. Basic projective properties for an imaged SOR. Property 2.1: Points x_i and x'_i correspond under \bar{W} ; all lines $x'_i \times x_i$ meet at $v_w \in l_s$. Property 2.2: Points y_i and y'_i correspond under H ; all lines $y'_i \times y_i$ meet at $v_\infty \in l_\infty$ (not shown in the figure).

Property 2.1. Any two imaged SOR cross sections are related to each other by a planar homology \bar{W} . The axis of this homology is the vanishing line l_∞ of the planes orthogonal to the SOR symmetry axis. The image of this axis, l_s , contains the vertex v_w of the homology [2], [1].

Property 2.2. The apparent contour of an imaged SOR is transformed onto itself by a harmonic homology H , the axis of which coincides with the imaged symmetry axis of the SOR, l_s . The vertex v_∞ of the homology lies on the aforementioned vanishing line l_∞ [16].

Denoting with C and C' , the 3×3 symmetric conic coefficient matrices associated with two generic cross sections that correspond pointwise under the planar homology \bar{W} , it holds $C' = \bar{W}^{-T} C \bar{W}$. The harmonic homology generalizes the usual concept of bilateral symmetry under perspective projection. In fact, the imaged axis of symmetry splits the imaged SOR in two parts, which correspond pointwise through H . This is true, in particular, for imaged cross sections that are fixed as a set under the harmonic homology: $C = H^{-T} C H$ (or $C = H^T C H$, being $H^{-1} = H$). To give an example, the two elliptical imaged cross sections C and C' of Fig. 2 are related by a planar homology \bar{W} with axis l_∞ and vertex v_w . The vertex v_w is always on the imaged axis of symmetry l_s . Imaged cross section points x_1, x_2, x_3 correspond to x'_1, x'_2, x'_3 under \bar{W} . Imaged cross section points x_1, x'_1, x_2, x'_2 also correspond, respectively, to x_3, x'_3, x_2, x'_2 under H . The points on the apparent contour y'_1, y'_2 correspond to y_1, y_2 under H . The lines through points y'_1, y_1 and y'_2, y_2 meet at v_∞ .

2.3 The Analogy between SOR Geometry and Single Axis Motion

Given a static camera, and a generic object rotating on a turntable, single axis motion (SAM) provides a sequence of different images of the object. This sequence can be imagined as being produced by a camera that performs a *virtual* rotation around the turntable axis while viewing a fixed object. Single axis motion can be described in terms of its *fixed entities*—i.e., those geometric objects in space or in the image that remain invariant throughout the sequence [3]. In particular, the imaged fixed entities can be used to express orthogonality

relations of geometric objects in the scene by means of the *image of the absolute conic* (IAC) ω —an imaginary point conic directly related to the camera matrix K as $\omega = K^{-T} K^{-1}$ [19].

Important fixed entities for the SAM are the imaged circular points i_π and j_π of the pencil of planes π orthogonal to the axis of rotation, and the horizon $l_\pi = i_\pi \times j_\pi$ of this pencil. The imaged circular points form a pair of complex conjugate points which lie on ω :

$$i_\pi^T \omega i_\pi = 0, \quad j_\pi^T \omega j_\pi = 0. \quad (2)$$

In practice, as i_π and j_π contain the same information, the two equations above can be written in terms of the real and imaginary parts of either points. Other relevant fixed entities are the imaged axis of rotation l_a and the vanishing point v_n of the normal direction to the plane passing through l_a and the camera center. These are in pole-polar relationship with respect to ω :

$$l_a = \omega v_n. \quad (3)$$

Equations (2) and (3) were used separately in the context of approaches to 3D reconstruction from turntable sequences. In particular, (2) was used in [15] and in [23] to recover metric properties for the pencil of parallel planes π given an uncalibrated turntable sequence. In both cases, reconstruction was obtained up to a 1D projective ambiguity, since the two linear constraints on ω provided by (2) were not enough to calibrate the camera. On the other hand, (3) was used in [52] to characterize the epipolar geometry of SAM in terms of l_a and v_n given a calibrated turntable sequence. Clearly, in this case, the a priori knowledge of intrinsic camera parameters allows one to obtain an unambiguous reconstruction. In the case of an SOR object, assuming that its symmetry axis coincides with the turntable axis, the apparent contour remains unchanged in every frame of the sequence. Therefore, for an SOR object, the fixed entities of the motion can be computed from any single frame of the sequence. According to this consideration, *an SOR image and a single axis motion sequence share the same projective geometry*: the fixed entities of SOR geometry correspond to the fixed entities of single axis motion. In particular,

1. l_a corresponds to l_s ;
2. v_n corresponds to v_∞ ;
3. (i_π, j_π) correspond to (i, j) ;
4. l_π corresponds to $l_\infty = i \times j$, where i and j denote the imaged circular points of the SOR cross sections.

Fig. 3 shows the geometrical relationships between the fixed entities and the image of the absolute conic. The analogy between SOR and SAM imaged geometry was exploited in [31] to locate the rotation axis and the vanishing point in SAM. It was also exploited in [55] to calibrate the camera from two SOR views under the assumption of zero camera skew. In that paper, the pole-polar relationship of l_s and v_∞ with respect to the image of the absolute conic was used to derive two constraints on ω . In Section 3.2, we will exploit the analogy one step forward and show that it is possible to apply both (2) and (3) to SORs for camera calibration and 3D reconstruction from a single SOR view.

3 THE APPROACH

In this section, we demonstrate that, given a single SOR view and assuming a zero skew/known aspect ratio camera (*natural camera*), the problems of camera calibration, metric

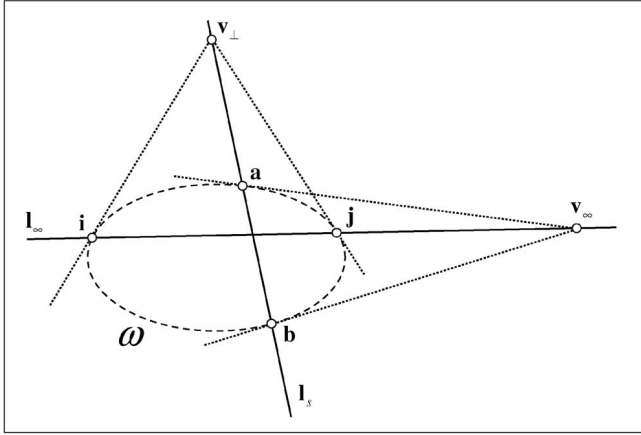


Fig. 3. The geometrical relationships between the fixed entities and the image of the absolute conic ω .

3D reconstruction, and texture acquisition are solved if the apparent contour γ and the visible segments of two distinct imaged cross sections C_1 and C_2 are extracted from the original image. Preliminary to this, we demonstrate that the fixed entities l_s , v_∞ , l_∞ , i , and j —that are required for all the later processing—can be unambiguously derived from the visible segments of the two imaged cross sections. This relaxes the conditions claimed by Jiang et al. in [23], where three ellipses are requested to compute the imaged circular points.

3.1 Derivation of the Fixed Entities

The nonlinear system

$$\begin{cases} \mathbf{x}^T C_1 \mathbf{x} = 0 \\ \mathbf{x}^T C_2 \mathbf{x} = 0 \end{cases} \quad (4)$$

that algebraically expresses the intersection between C_1 and C_2 has four solutions \mathbf{x}_k , $k = 1 \dots 4$ —of which no three are collinear [43]—that can be computed as the roots of a quartic polynomial [41]. At least two solutions of the system of (4) are complex conjugate and coincide with the imaged circular points i and j , which are the intersection points of any imaged cross section with the vanishing line l_∞ . According to this, the remaining two solutions are either real or complex conjugate.

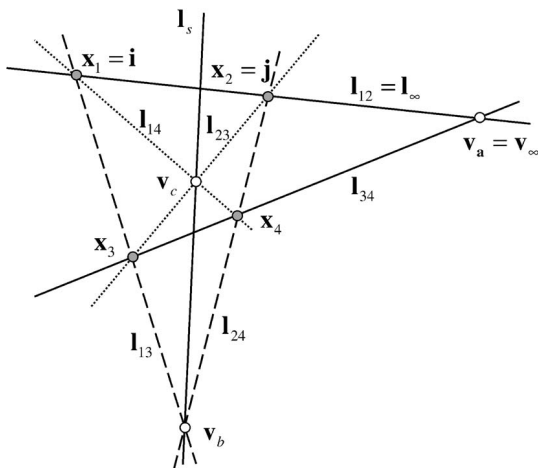


Fig. 4. Geometric properties of the four intersection points of C_1 and C_2 with the hypothesis $l_\infty = l_{12}$.

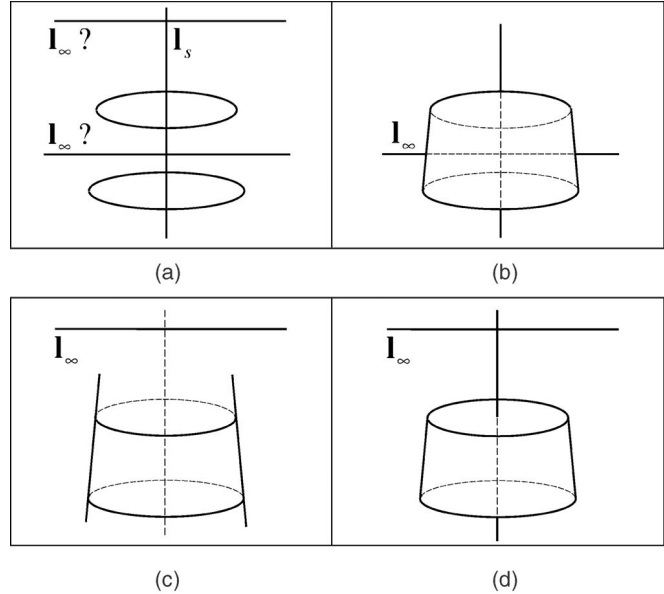


Fig. 5. (a) Two imaged cross sections (b), (c), and (d) and their possible interpretations. The twofold ambiguity in the determination of the vanishing line can be solved by exploiting the visibility conditions. Visible contours are in bold.

In the following, we will assume, without loss of generality, that the solutions \mathbf{x}_1 and \mathbf{x}_2 are complex conjugate.

Fig. 4 shows the geometric construction for the derivation of the fixed entities v_∞ and l_s . The four solutions \mathbf{x}_k s form a so called “complete quadrangle” and are represented in the figure by the filled-in circles. In the figure it is assumed that \mathbf{x}_1 and \mathbf{x}_2 are the two imaged circular points i and j . The \mathbf{x}_k s may be joined in pairs in three ways through the six lines $l_{ij} = \mathbf{x}_i \times \mathbf{x}_j$, $i = 1, \dots, 3$, $j = i + 1, \dots, 4$. Each pair of lines has a point of intersection and the three new points (hollow circles in the figure) form the vertices of the so called “diagonal triangle” associated with the complete quadrangle. The vertex of the harmonic homology v_∞ is the vertex of the diagonal triangle which lies on the line l_{12} connecting the two complex conjugate points \mathbf{x}_1 and \mathbf{x}_2 . The imaged axis of symmetry l_s is the line connecting the remaining two vertices of the diagonal triangle. In particular, the vertex of the harmonic homology and the imaged axis of symmetry can be computed, respectively, as

$$v_\infty = l_{12} \times l_{34} \quad (5)$$

and

$$l_s = (l_{13} \times l_{24}) \times (l_{14} \times l_{23}). \quad (6)$$

The proof of this result is given in Appendix A.

The computation of the vanishing line l_∞ is straightforward when the two solutions \mathbf{x}_3 and \mathbf{x}_4 are real. In this case, \mathbf{x}_1 and \mathbf{x}_2 are the imaged circular points and, by consequence, $l_\infty = l_{12}$. On the other hand, when \mathbf{x}_3 and \mathbf{x}_4 also are complex conjugate, an ambiguity arises in the computation of l_∞ , since both l_{12} and l_{34} are physically plausible vanishing lines. In fact, a pair of imaged cross sections C_1 and C_2 with no real points of intersection are visually compatible with two distinct views of the planar cross sections, where each view corresponds to a different vanishing line. Fig. 5a shows an example of two imaged cross sections and the two possible solutions for the vanishing line; Fig. 5b shows the correct solution for the vanishing line when the camera center is at

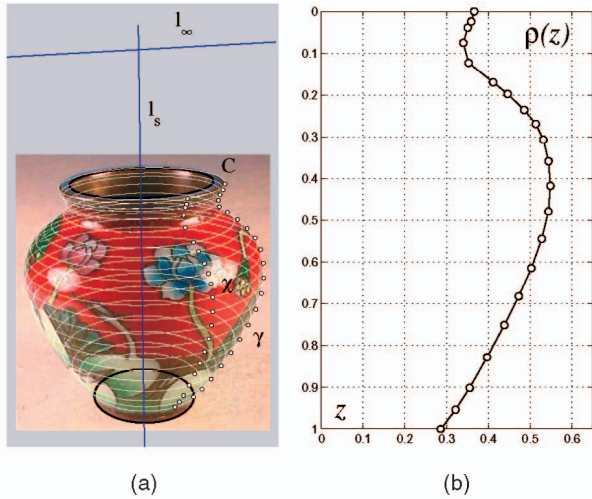


Fig. 7. (a) Recovery and (b) rectification of an imaged meridian.

As shown in Fig. 6, given the apparent contour γ , there exists a unique imaged cross section C' that includes the generic point $\mathbf{x}'_\gamma \in \gamma$. Correspondingly, once the vanishing line l_∞ is given, there exists a unique planar homology W that maps a reference imaged cross section C onto C' . As \mathbf{x}'_γ varies on γ , the vertex \mathbf{v}_W and the characteristic invariant μ_W of W also vary, while l_∞ remains fixed. Therefore, as $\mathbf{x}'_\gamma \in C'$ is moved along γ , it gives rise to a family of planar homologies $W: C \rightarrow C'$.

We now show how to compute the planar homology W at a given \mathbf{x}'_γ . According to Property 3.1, there exists an imaged cross section C' such that γ and C' share the same tangent line l' at \mathbf{x}'_γ . The tangent line l' intersects the vanishing line l_∞ at the point \mathbf{u}_∞ : According to Property 3.2, this is the vanishing point of all the lines which are tangent to the SOR along the same meridian. Therefore, the tangent line l to C from \mathbf{u}_∞ meets C at the point \mathbf{x} such that $\mathbf{x}'_\gamma = W\mathbf{x}$ and the planar homology vertex \mathbf{v}_W is the point where the line through \mathbf{x} and \mathbf{x}'_γ intercepts the imaged axis of symmetry l_s :

$$\mathbf{v}_W = (\mathbf{x} \times \mathbf{x}'_\gamma) \times \mathbf{l}_s. \quad (8)$$

This fixes two of the three degrees of freedom left for W . The remaining degree of freedom is fixed by computing the characteristic invariant μ_W as

$$\mu_W = \{\mathbf{v}_W, \mathbf{w}_\infty, \mathbf{x}, \mathbf{x}'_\gamma\}, \quad (9)$$

where $\mathbf{w}_\infty = (\mathbf{x} \times \mathbf{x}'_\gamma) \times \mathbf{l}_\infty$ is the point where the line through \mathbf{x} and \mathbf{x}'_γ intercepts the vanishing line l_∞ , and $\{\}$ denotes the usual cross ratio of four points [43].

For each W that is obtained from the steps above, by exploiting the Property 3.3, a point \mathbf{x}'_χ on the imaged meridian χ that passes through the point $\mathbf{x}_\chi \in C$ is computed as $\mathbf{x}'_\chi = W\mathbf{x}_\chi$. The imaged meridian χ is then recovered as the set of all the points \mathbf{x}'_χ obtained for different points \mathbf{x}'_γ sampled on the apparent contour (see Fig. 7a).

3.3.2 Rectification of the Imaged Meridian

The rectification of χ requires the availability of both the image of the absolute conic ω and the vanishing line \mathbf{m}_∞ of the plane π_χ through the meridian and the SOR symmetry axis.

As this axis lies by construction on π_χ , once the rectifying homography M_r for this plane is known, we are able to

rectify both the imaged meridian χ and the imaged axis of symmetry l_s according to

$$\begin{cases} \mathbf{x}_\rho = M_r \mathbf{x}'_\chi \\ \mathbf{l}_z = M_r^{-T} \mathbf{l}_s. \end{cases} \quad (10)$$

By computing the distance between any point \mathbf{x}_ρ and the line l_z , it is then possible to obtain the values of z and $\rho(z)$ for each \mathbf{x}'_χ given the reference SOR axis l_s (see Fig. 7b).

The vanishing line \mathbf{m}_∞ can be obtained as $\mathbf{m}_\infty = \mathbf{x}_\infty \times \mathbf{v}_\perp$, where \mathbf{x}_∞ and \mathbf{v}_\perp are, respectively, the vanishing point of the direction of all lines in π_χ that are orthogonal to the SOR symmetry axis, and the vanishing point of the direction of the same axis (see Fig. 6). The vanishing point \mathbf{x}_∞ is computed as

$$\mathbf{x}_\infty = (\mathbf{x}_\chi \times \mathbf{o}) \times \mathbf{l}_\infty = (\mathbf{x}_\chi \times C^{-1} \mathbf{l}_\infty) \times \mathbf{l}_\infty, \quad (11)$$

where $\mathbf{o} = C^{-1} \mathbf{l}_\infty$ is the image of the center of the cross section that projects onto C ; this point is in pole-polar relationship with l_∞ with respect to C . Since ω is known, the vanishing point \mathbf{v}_\perp can be computed as $\mathbf{v}_\perp = \omega^{-1} \mathbf{l}_\infty$. The vanishing line \mathbf{m}_∞ can now be intersected with ω in order to obtain the imaged circular points \mathbf{i}_χ and \mathbf{j}_χ . This intersection can be algebraically computed by solving for λ the quadratic equation $(\mathbf{x}_\infty + \lambda \mathbf{v}_\perp)^T \omega (\mathbf{x}_\infty + \lambda \mathbf{v}_\perp) = 0$, where $\mathbf{x}_\infty + \lambda \mathbf{v}_\perp$ denotes the generic point on \mathbf{m}_∞ . The required imaged circular points are obtained from the two complex conjugate solutions λ_1 and λ_2 , respectively, as $\mathbf{i}_\chi = (\mathbf{x}_\infty + \lambda_1 \mathbf{v}_\perp)$ and $\mathbf{j}_\chi = (\mathbf{x}_\infty + \lambda_2 \mathbf{v}_\perp)$. According to [29], the rectifying homography for the plane π_χ is

$$M_r = \begin{pmatrix} \beta^{-1} & -\alpha \beta^{-1} & 0 \\ 0 & 1 & 0 \\ m_1 & m_2 & 1 \end{pmatrix}, \quad (12)$$

where $\mathbf{m}_\infty = (m_1, m_2, 1)$ and $\mathbf{i}_\chi = \text{conj}(\mathbf{j}_\chi)$ is expressed as $M_r^{-1}(1, i, 0) = (\alpha - i\beta, 1, -m_2 - m_1\alpha + im_1\beta)$.

3.3.3 Discussion

The above two-step method for 3D metric reconstruction is equivalent to the computation of the set of pairs $\{(z, \rho(z))\}$, where z is the point of the SOR symmetry axis that corresponds to a point \mathbf{x}'_γ sampled on the apparent contour γ . This correspondence can be expressed in terms of a function $\zeta: \gamma \rightarrow [0, 1]$ such that

$$z = \zeta(\mathbf{x}'_\gamma). \quad (13)$$

The function ζ is defined only at points \mathbf{x}'_γ at which γ is smooth and has a unique tangent line. These points belong to a unique imaged cross section C' , whose corresponding pair $(z, \rho(z))$ can then be correctly recovered with the method above. In the presence of self-occlusions, the apparent contour can have singular points at which γ is not smooth and has two distinct tangent lines. The values z_- and z_+ corresponding to the two tangent lines at a singular point delimit the portion of the z axis at which no $\rho(z)$ can be computed with the method above. In this case, the method still guarantees that the scaling function be correctly recovered piecewise as a nonconnected curve.

If a uniform sampling strategy for γ is used, a nonuniform sampling of z is obtained. Conversely, if a uniform sampling on the z axis is required, then the inverse of ζ should be used. However, according to the definition of γ used so far, the function ζ is not invertible. In fact, the apparent contour is split by the imaged axis of symmetry into two halves, the

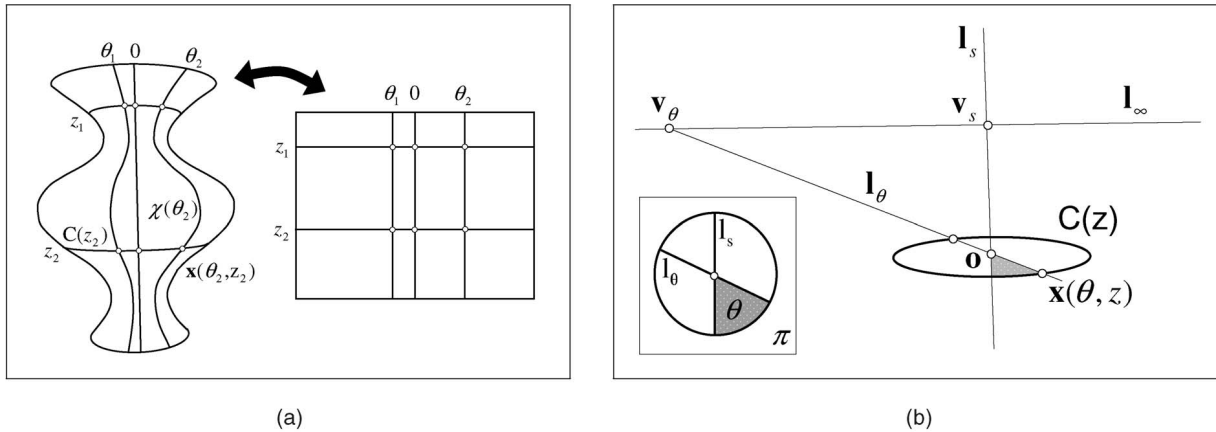


Fig. 8. (a) The geometry of SOR texture acquisition. Meridians and parallels in the image plane (left) are mapped into mutually orthogonal lines in the texture plane (right). (b) Sampling an imaged cross section $C(z)$ at a given Euclidean angle θ .

points of which correspond in pairs under the harmonic homology. The two points of a pair carry the same reconstruction information, since both of them are mapped by ζ onto the same z . Without loss of generality, we can restrict the domain of ζ to one of two halves of γ , say γ' , so as to ensure that the function $\zeta^{-1} : [0, 1] \rightarrow \gamma'$ exists. This maps any point z at which the value $\rho(z)$ can be recovered with the method above onto a single point $\mathbf{x}'_{\gamma'}$ of the apparent contour. The computation of $\mathbf{x}'_{\gamma'} = \zeta^{-1}(z)$ at the generic z is carried out using a recursive subdivision scheme similar to the one proposed in [14].

A uniform sampling on the z axis can be conveniently used for texture acquisition, as discussed in the following section.

3.4 Texture Acquisition

As shown in Fig. 8a, the SOR texture is the rectangular image $T(\theta, z) = I(\mathbf{x}(\theta, z))$, where I is the image function and $\mathbf{x}(\theta, z)$ is the image projection of the 3D point $\mathbf{P}(\theta, z)$ parametrized as in Section 2.1.

Texture acquisition following the canonical parameterization (θ, z) can be solved through the well-known cartographic method of *normal cylindrical projection* [5]. However, if parallels and meridians of the imaged object are sampled at regular (θ, z) in the Euclidean space, a nonuniform sampling of the texture is created. In order to avoid this, we follow the inverse method (from a regular grid of (θ, z) on the texture plane to points on the image plane) that assures that a uniformly sampled texture is created.

To obtain a metric texture, θ and z are therefore sampled at regular intervals. The resulting texture image has M rows and N columns. The unknown image point $\mathbf{x}(\theta, z)$ is the intersection between the imaged meridian $\chi(\theta)$ corresponding to the SOR meridian at θ and the visible portion of the imaged parallel $C(z)$ corresponding to the SOR parallel at z . Therefore, the rows of the texture image are composed of image pixels sampled from $C(z)$ at regular intervals of θ .

A method to sample the visible portion of an imaged parallel $C(z)$ at a given value of the Euclidean angle θ is described in Appendix C. The method permits Laguerre's formula [13]

$$\theta = \frac{1}{2i} \log(\{\mathbf{v}_\theta, \mathbf{v}_s, \mathbf{i}, \mathbf{j}\}) \quad (14)$$

to be inverted so as to compute the vanishing point \mathbf{v}_θ and to obtain, from this, the sampled point $\mathbf{x}(\theta, z)$ —see Fig. 8b.

The algorithm for the computation of a generic texture row $\{T(\theta, z), \theta = \theta_1, \dots, \theta_N\}$ is:

1. Choose a reference imaged parallel C .
2. Compute $\mathbf{x}'_{\gamma'} = \zeta^{-1}(z)$ as shown in Section 3.3.3.
3. Use the planar homology W associated to $\mathbf{x}'_{\gamma'}$ (see Section 3.3.1) to compute the imaged parallel $C' = W^{-T}CW^{-1}$.
4. Sample C' at all values $\theta = \theta_1, \dots, \theta_N$ as described in Appendix C.
5. For each of the N points, $\mathbf{x}'_{\chi(\theta)} = \mathbf{x}(\theta, z)$ thus obtained, set $T(\theta, z) = I(\mathbf{x}'_{\chi(\theta)})$.

Texture acquisition is achieved by repeating steps 1 through 4 for all the M rows of the texture image, sampled at regular intervals of z .

It is worth noting that not all the texture image pixels can be computed by the algorithm above. In particular, singular points on the apparent contour γ' due to self-occlusions give rise to row intervals $[z_-, z_+]$ for which the inverse function $\zeta^{-1}(z)$ cannot be computed (see Section 3.3.3). A similar situation occurs for the range of θ values for which the surface is not visible. In this case, for each imaged parallel $C(z)$, Laguerre's formula—with the value \mathbf{u}_∞ of Section 3.2.1 used in (14) in the place of \mathbf{v}_θ —can be used to determine the interval $[\theta_{\min}(z), \theta_{\max}(z)]$ for which the parallel is visible.

The method for texture acquisition described above has some advantages over other solutions presented in the literature. It uses a 2D/2D point transformation applied to SOR pixels that requires only the knowledge of internal camera parameters. This way, a higher accuracy is obtained than with 2D/3D registration methods [22], which back-project the image data onto the 3D object and require both the internal and external camera parameters to fully recover the camera mapping $\mathbf{P}(\theta, z) \rightarrow \mathbf{x}(\theta, z)$. Moreover, since *inverse texture mapping* is used, the method avoids “holes” in the texture image due to insufficient sampling of the image space, a typical drawback of direct texture mapping methods [21], which compute the transformation $\mathbf{x}(\theta, z) \rightarrow (\theta, z)$.

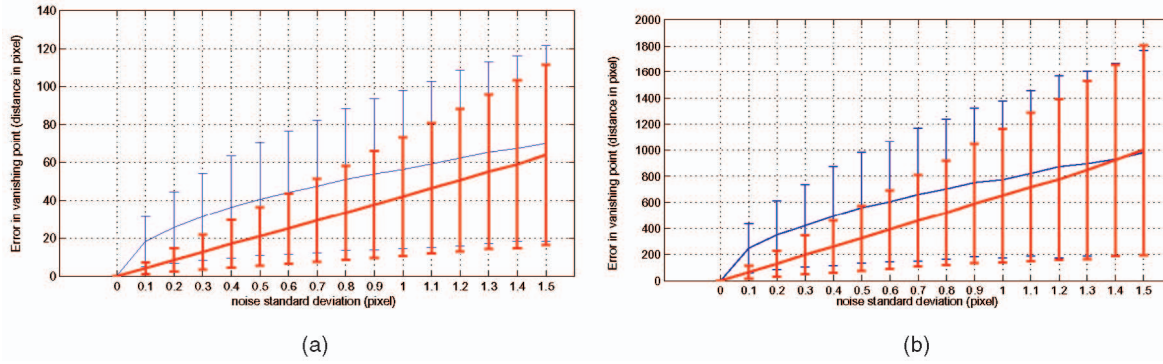


Fig. 9. Vanishing point estimation accuracy in (a) nondegeneracy view condition (ground truth: $v_\infty = (3421.978, 209.049, 1)$) and (b) near degeneracy view condition (ground truth: $v_\infty = (12493.024, 206.432, 1)$). Different scales are used in the two charts.

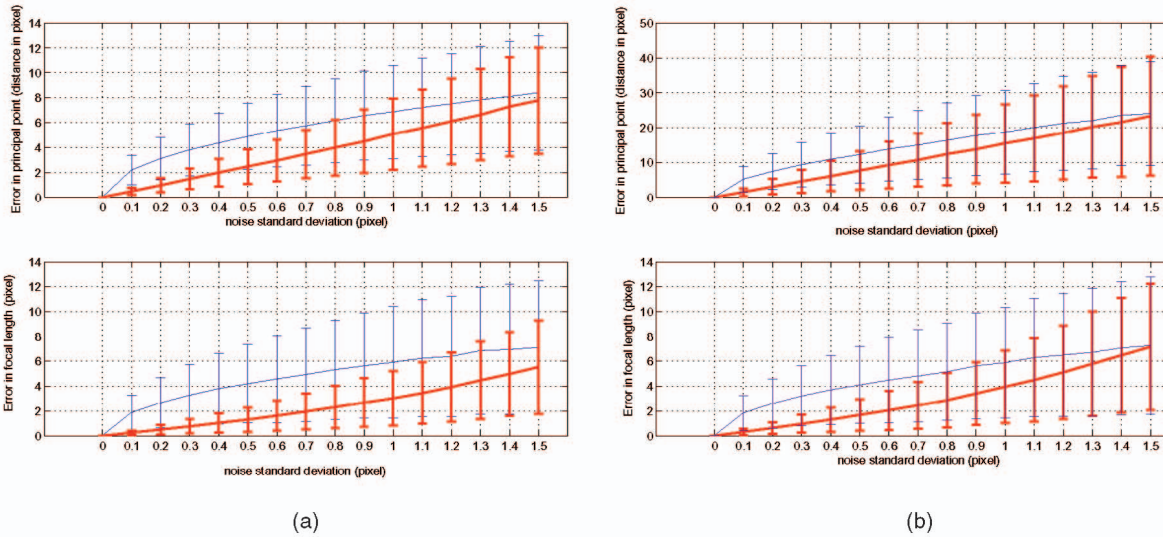


Fig. 10. Self-calibration accuracy in (a) nondegeneracy and (b) near degeneracy view conditions. Top: principal point estimation (ground truth: $(u_0, v_0) = (400, 300)$). Bottom: focal length estimation (ground truth: $f = 750$).

4 IMPLEMENTATION AND EXPERIMENTAL RESULTS

4.1 Accuracy Evaluation

Several experiments were performed in order to test the accuracy of the approach. In particular, we assessed the accuracy of vanishing point estimation, camera self-calibration, and reconstruction of the SOR scaling function. Two different views of the synthetic object of Fig. 1—generated by the scaling function $\rho_{gt}(z) = \frac{1}{10}(\cos(\frac{\pi}{2}(\frac{19}{3}z + 1)) + 2)$ with $z \in [0, 1]$ —were taken using a virtual camera with internal parameters: focal length $f = 750$ (simulating a wide angle lens) and principal point coordinates $(u_0, v_0) = (400, 300)$. The two views, referred to as *nondegeneracy view* and *near degeneracy view*, were obtained by panning the virtual camera, around an axis parallel to the SOR symmetry axis, by 14.0 and 3.5 degrees, respectively. The *degeneracy view* condition in which the imaged SOR symmetry axis coincides with the vertical image axis passing by the principal point is taken as the reference camera position. In all the experiments, the points of the imaged cross sections and apparent contour of the SOR, sampled at the same resolution as that of the image, were corrupted by a white, zero mean Gaussian noise with standard deviation between 0 and 1.5 pixel. The influence of this noise was tested by running a Monte Carlo simulation with 10,000 trials for each of the parameters under test.

Fig. 9 shows the accuracy of vanishing point estimation (the most noise-sensitive fixed entity), for the two cases of

nondegeneracy (Fig. 9a) and near degeneracy (Fig. 9b). Mean and standard deviation of the estimation error are represented, respectively, as light lines and vertical bars ($\pm 1\sigma$). The two quantities grow almost linearly with noise. The bias for nonzero noise values is due to the use of an algebraic distance rather than a geometric one in the estimation of ellipses. The accuracy of the estimation in the nondegeneracy condition is higher by about one order of magnitude than in the near degeneracy condition. Bold curves and bars indicate a reference condition where all the points of the imaged cross sections are available. It can be noticed that, in noisy conditions, the accuracy obtained when a subset of the points of the imaged cross sections is used, is approximately that obtained in the case in which all the points are available.

Self-calibration accuracy is shown in Fig. 10 for the two viewing conditions. Top figures show accuracy in principal point estimation; the bottom figures show accuracy in focal length estimation. In the nondegeneracy case (Fig. 10a), the principal point is estimated with an error less than 10 pixels, even in the presence of high noise; a higher error value is always observed in the near degeneracy case (Fig. 10b). In noisy conditions, bold and light curves exhibit the same behavior as in the case of vanishing point estimation. Besides, focal length estimation accuracy has proven to be less dependent on camera viewpoint than principal point estimation accuracy.

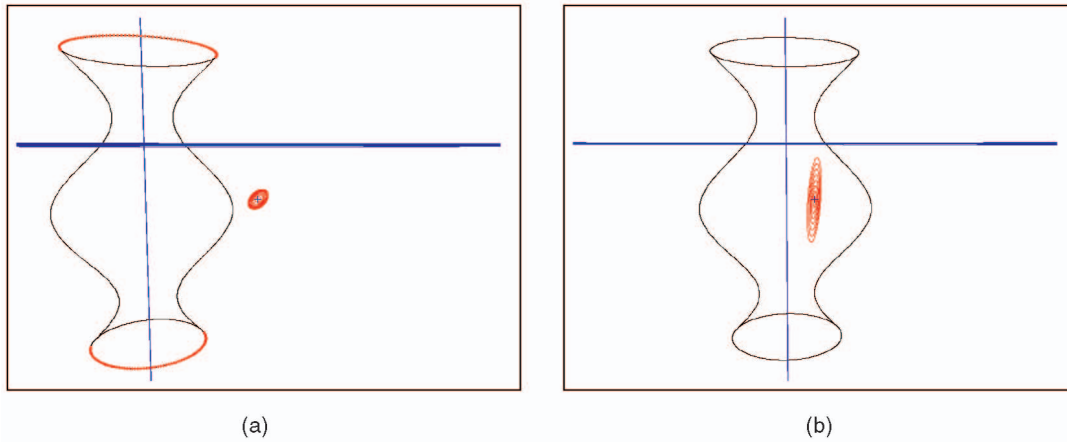


Fig. 11. A sample SOR with a qualitative view of calibration uncertainty (ellipses), for different noise values, in the two cases of nondegeneracy (a) and near degeneracy (b) view conditions.

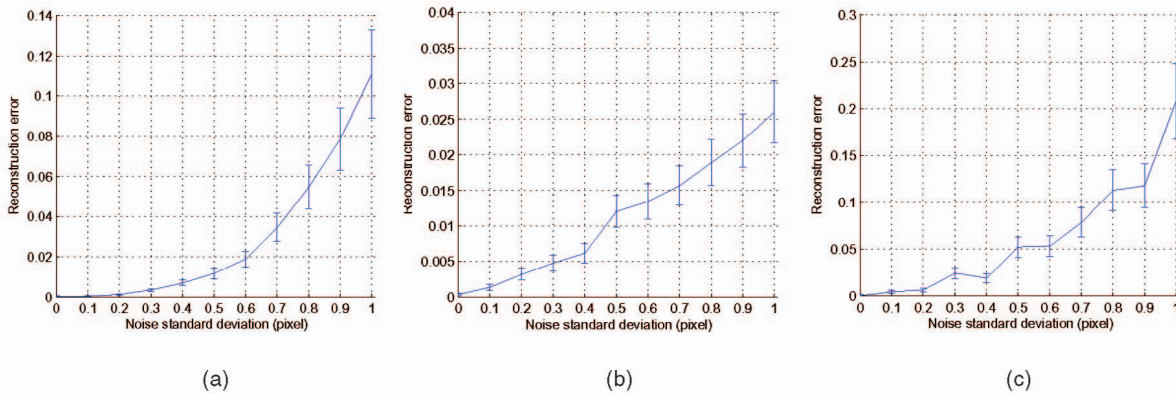


Fig. 12. Reconstruction accuracy in the near degeneracy case. (a) Noisy apparent contour (max standard deviation = 0.0218). (b) Noisy visible points of imaged cross sections (max standard deviation = 0.0043). (c) Noisy apparent contour and noisy visible points of imaged cross sections (max standard deviation = 0.0395). The maximum value of standard deviation is obtained for the maximum noise value.

A qualitative insight into principal point estimation accuracy is provided by Fig. 11, where uncertainty 3σ ellipses are drawn for different noise values. It is apparent that, as the SOR position in the image gets closer to the image center, the uncertainty ellipses become larger, with their major axis parallel to the imaged symmetry axis. In fact, in the pure degeneracy condition, an infinite uncertainty affects the principal point coordinate along the imaged symmetry axis.

The mean and standard deviation of the error in the reconstruction of the scaling function are defined, respectively, as $\int_0^1 |\rho_e(z) - \rho_{gt}(z)| dz$ and $\sqrt{\int_0^1 [\rho_e(z) - \rho_{gt}(z)]^2 dz}$, where $\rho_e(z)$ is the estimated scaling function, and $\rho_{gt}(z)$ is the ground truth scaling function. Fig. 12 shows the effects of noise on the reconstruction error in the near degeneracy case (the most critical one). The noise on the apparent contour is the dominant source of error for reconstruction, due to the fact that it requires the computation of tangent lines along the apparent contour.

4.2 Creation of 3D Textured Models

Fig. 13 shows examples of reconstruction from a single uncalibrated view for four distinct SOR objects. For each object, the original image and the 3D solid obtained are shown. All the images have been taken with moderate perspective distortion. The apparent contour and cross

sections have been manually extracted by following the imaged object's boundaries. The results presented can therefore be regarded as close to those obtainable in the absence of noise.

Figs. 13a, 13b, and 13c present objects with linear (Fig. 13a) and curvilinear (Figs. 13b and 13c) profiles (a can, and a Chinese and Greek vase, respectively). For each object, both the uncalibrated view (top) and a view of the reconstructed solid object (bottom) are shown. Three-dimensional objects are correctly reconstructed in all the cases. Fig. 13d presents the case in which 3D reconstruction of the original object (a transparent glass) would have been difficult with a laser scanner, due to the object's physical properties. It can be observed (bottom) that the 3D model is correctly reconstructed from the original view (top).

Fig. 14 shows the case of a drawing of which there is not any physical reproduction. It displays the first "wireframe" drawing in history, made by the Renaissance artist Paolo Uccello (Fig. 14a) and two views of the reconstructed 3D model (Figs. 14b and 14c). Since the wireframe drawing provides information also for the occluded parts of the apparent contour, a more complete reconstruction of the object model can be obtained.

Fig. 15 presents two critical cases for 3D SOR reconstruction, respectively, due to strong perspective distortion (Fig. 15a) and the presence of self-occlusions (Fig. 15b). Fig. 15a, middle shows that the scaling function of the bottle is correctly recovered: The ratio of the bottom and top radii of



Fig. 13. SOR objects: (top) single uncalibrated views and (bottom) reconstructed 3D models.

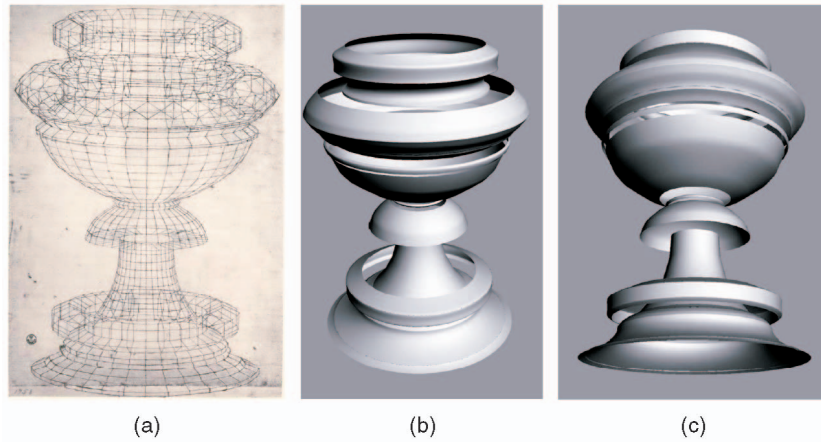


Fig. 14. (a) Wireframe drawing of a chalice by Paolo Uccello (1397-1475). (b) and (c) Two views of the reconstructed model, with evidence of self-occluded parts.

the reconstructed bottle differs by less than 3 percent from the real one. In Fig. 15b, left the segments $\gamma_1, \gamma_2, \gamma_3, \gamma_4$ of the apparent contour of the cup are shown, that are related to curve singularities due to self-occlusions. Fig. 15b, right shows that, for each apparent contour segment, the corresponding scaling function segments $\rho_1, \rho_2, \rho_3, \rho_4$ can be obtained so that a 3D (partial) reconstruction is still possible for which the global metric structure of the reconstructed SOR object is preserved.

4.3 Texture Acquisition

The acquisition of the flattened texture permits the complete three-dimensional reconstruction of the visible part of the SOR object as well as a separate analysis of the true texture properties, regardless of the perspective distortion. Texture flattening makes image details more evident than in the original picture and also gives the same importance to central and peripheral details. Fig. 16 shows the flattened texture acquired from the image of the Greek vase of Fig. 13. In this case, the original texture is applied to a quasispherical surface. While areas are locally preserved, the flattening

process has introduced distortions in all those parts of the surface the shape of which differs locally from that of a cylinder coaxial with the SOR. Fig. 17a shows the case of texture acquisition for a cylindrical surface (the can in Fig. 13). As the cylinder is a developable surface, the flattened texture preserves the global geometry of the original surface. This allows the recovery of the hexagonal "AL" mark, by removing the distortion present in the original image. The texture portions close to the apparent contour have not been considered, in that their resampling is typically affected by aliasing due to the strong foreshortening. Foreshortening effects are clearly visible in Fig. 17b, where the complete flattened texture for the Chinese vase of Fig. 13 is shown, including the texture portions close to the apparent contour. Flattened textures can be easily superimposed on the reconstructed 3D model, so as to obtain photorealistic reconstructions from image data. Fig. 18 shows the reconstructed 3D can and Chinese vase models of Fig. 13 with their flattened textures superimposed.

Fig. 19, top shows four different views of a Japanese vase that together provide complete information of the vase



Fig. 15. (a) Left: An SOR view taken under strong perspective conditions (with indications of the two cross section C_1 and C_2 , the apparent contour γ and the projection of the SOR meridian χ). Middle: The SOR scaling function rectified. Right: The reconstructed 3D model. (b) Left: A SOR view with severe self-occlusion and its apparent contour. Right: The partially reconstructed scaling function.



Fig. 16. Flattened texture from the image of the archaeological vase of Fig. 13. Surface region with the largest distortion are indicated with circles.

texture. If a flattened texture is extracted from each view and the 3D vase structure is reconstructed from one view, a 3D fully textured reconstruction of the vase can be obtained as in Fig. 20 provided that the complete texture is constructed by registration of the four textures (see Fig. 19, bottom). Similarly, partially reconstructed scaling functions obtained from different self-occluded views can be merged together so as to obtain a full 3D SOR model.

5 CONCLUSIONS

In this paper, we have discussed a new method to recover the original 3D structure of a generic SOR object and its texture from a single uncalibrated view. The solution proposed exploits projective properties of imaged SORs, expressed through planar and harmonic homologies. Camera self-calibration is directly obtained from the analysis of the visible elliptic segments of two imaged cross sections of the SOR. The same elliptic segments are used together with the SOR apparent contour, to reconstruct the 3D structure and texture of the SOR object, which are thus obtained from calculations in the 2D domain. Since the homology constraints are of general applicability, the solution can be applied under full perspective conditions to any type of surface of revolution with at least two partially visible cross sections. According to this, the method provides an advancement with respect to recent research contributions that used homology constraints for 3D recognition/reconstruction, but were restricted to the affine projection case [1] or to full perspective of planar

surfaces [27], [46]. The possibility of recovering the texture superimposed on the SOR as a flattened image allows a complete reconstruction (albeit limited to the imaged part of the object) of the SOR 3D structure and appearance. For views with self-occlusions, a complete reconstruction of the 3D textured object can be easily obtained by registration of multiple views of the SOR, taken from the same camera under the same illumination conditions. The method can be used reliably, in all those cases in which only a photograph or a drawing of the SOR object is available and structured light acquisition methods cannot be employed for the acquisition



Fig. 17. (a) The flattened textures for the can and (b) the Chinese vase of Fig. 13.



Fig. 18. (a) Three-dimensional reconstruction of the can and (b) Chinese vase models with superimposed texture.

of the solid structure. It is particularly useful in the case of no longer existing objects (i.e., artworks) or objects that cannot be moved easily from their original site. Extraction of the apparent contour and imaged cross section segments, although done manually in the experiments reported in this

paper, can also be performed automatically, with relatively low complexity and good reliability. This has been proposed in [57] and [7] under reasonable constraints on the objects and background.

APPENDIX A

RELATING THE HARMONIC HOMOLOGY WITH THE COMPLETE QUADRANGLE

In this appendix, we give the formal proof of (5) and (6) used to compute the fixed entities of the harmonic homology H from the four intersections $x_k, k = 1, \dots, 4$ of two imaged cross sections C_1 and C_2 . Following the discussion of Section 3.1, we can always assume that x_1 and x_2 are complex conjugate, so that either of the pairs (x_1, x_2) or (x_3, x_4) must be equal to (i, j) and, therefore, either of the lines $l_{12} = x_1 \times x_2$ or $l_{34} = x_3 \times x_4$ must be equal to $l_\infty = i \times j$.

By Property 2.2 of Section 2.2, the conics C_1 and C_2 are fixed as a set under the harmonic homology: $C_h = H^T C_h H, h = 1, 2$. A consequence of this is that the point Hx_k obtained from the generic intersection point x_k by transformation under H , is still an intersection point of C_1 and C_2 : $(Hx_k)^T C_h (Hx_k) = 0, h = 1, 2$. By expressing H according to the parametrization



Fig. 19. Top: Four complementary views of a Japanese vase. Bottom: The complete texture obtained by image registration.



Fig. 20. Three views of the complete (3D structure and texture) three-dimensional reconstruction of the Japanese vase.

$$\mathbf{H} = \mathbf{I} - 2 \frac{\mathbf{v}_\infty \mathbf{l}_s^T}{\mathbf{v}_\infty^T \mathbf{l}_s} \quad (15)$$

obtained from (1) with $\mu = -1$, we can write

$$\mathbf{H}\mathbf{x}_k = \mathbf{x}_k - 2 \frac{\mathbf{l}_s^T \mathbf{x}_k}{\mathbf{l}_s^T \mathbf{v}_\infty} \mathbf{v}_\infty. \quad (16)$$

Now, since by (16) the line $\mathbf{x}_k \times \mathbf{H}\mathbf{x}_k$ must contain the fixed point \mathbf{v}_∞ , recalling that $(\mathbf{i} \times \mathbf{j})^T \mathbf{v}_\infty = 0$ and that no three intersection points can be collinear, it follows that

$$\mathbf{x}_2 = \mathbf{H}\mathbf{x}_1 \text{ and } \mathbf{x}_4 = \mathbf{H}\mathbf{x}_3. \quad (17)$$

This proves (5), since as the lines \mathbf{l}_{12} and \mathbf{l}_{34} can be written, respectively, as $\mathbf{x}_1 \times \mathbf{H}\mathbf{x}_1$ and $\mathbf{x}_3 \times \mathbf{H}\mathbf{x}_3$. Using (15), we can also write $\mathbf{l}_{13} \times \mathbf{l}_{24} = (\mathbf{x}_1 \times \mathbf{x}_3) \times (\mathbf{H}\mathbf{x}_1 \times \mathbf{H}\mathbf{x}_3)$ and $\mathbf{l}_{14} \times \mathbf{l}_{23} = (\mathbf{x}_1 \times \mathbf{H}\mathbf{x}_3) \times (\mathbf{H}\mathbf{x}_1 \times \mathbf{x}_3)$. By using, again, the parametrization of (15) and the basic equality $\mathbf{a} \times (\mathbf{b} \times \mathbf{c}) = (\mathbf{a}^T \mathbf{c})\mathbf{b} - (\mathbf{a}^T \mathbf{b})\mathbf{c}$, it follows easily that $\mathbf{l}_{13} \times \mathbf{l}_{24} = \mathbf{l}_{13} \times \mathbf{l}_s$ and $\mathbf{l}_{14} \times \mathbf{l}_{23} = \mathbf{l}_{14} \times \mathbf{l}_s$. This proves (6).

APPENDIX B

PARAMETRIZING THE IMAGE OF THE ABSOLUTE CONIC

In this appendix, we demonstrate that the linear system of (7) has only three independent constraints, and provide a parametrization for the ∞^2 conics that satisfy these constraints.

The third of (7) provides two independent linear constraints on ω . We will show that the first two equations of the system, i.e., $\mathbf{i}^T \tilde{\omega} \mathbf{i} = 0$ and $\mathbf{j}^T \tilde{\omega} \mathbf{j} = 0$, add to $\mathbf{l}_s = \omega \mathbf{v}_\infty$ only one independent constraint. Indeed, the family of ∞^3 conics $\tilde{\omega}$ satisfying $\mathbf{l}_s = \tilde{\omega} \mathbf{v}_\infty$ can be written as

$$\tilde{\omega}(\lambda_1, \lambda_2, \lambda_3) = \Lambda_0 + \sum_{k=1}^3 \lambda_k \Lambda_k, \quad (18)$$

where the λ_k s are scalars and the Λ_k s are four linearly independent conics such that

$$\mathbf{l}_s = \Lambda_k \mathbf{v}_\infty. \quad (19)$$

Now, in Appendix A, we have shown that $\mathbf{j} = \mathbf{H}\mathbf{i}$. Therefore, we can write

$$\mathbf{j}^T \Lambda_k \mathbf{j} = \mathbf{i}^T (\mathbf{H}^T \Lambda_k \mathbf{H}) \mathbf{i} = \mathbf{i}^T \Lambda_k \mathbf{i}, \quad (20)$$

where the last equality follows from the fact that, as it satisfies (19), each of the Λ_k s is transformed onto itself by the homology \mathbf{H} —this can also be directly verified by using for \mathbf{H} the parametrization of Appendix A. From (2), it also follows that $\mathbf{j}^T \tilde{\omega} \mathbf{j} = \mathbf{i}^T \tilde{\omega} \mathbf{i}$: this means that the inhomogeneous linear system in the three unknowns λ_k s

$$\begin{cases} \mathbf{i}^T \tilde{\omega}(\lambda_1, \lambda_2, \lambda_3) \mathbf{i} = 0 \\ \mathbf{j}^T \tilde{\omega}(\lambda_1, \lambda_2, \lambda_3) \mathbf{j} = 0 \end{cases} \quad (21)$$

has ∞^2 solutions. This proves our assertion that the solution set of (7) is composed of ∞^2 conics. It can be easily verified that a valid parametrization for these conics is

$$\tilde{\omega}(p, q) = \omega + p \mathbf{l}_\infty \mathbf{l}_\infty^T + q (\mathbf{l}_{is} \mathbf{l}_{js}^T + \mathbf{l}_{js} \mathbf{l}_{is}^T), \quad (22)$$

where ω is the (unknown) true image of the absolute conic, $\mathbf{l}_\infty \mathbf{l}_\infty^T$ is a degenerate (rank 1) conic composed by the line \mathbf{l}_∞ taken twice, and $\mathbf{l}_{is} \mathbf{l}_{js}^T + \mathbf{l}_{js} \mathbf{l}_{is}^T$ is a degenerate (rank 2) conic composed by the two lines $\mathbf{l}_{is} = \mathbf{i} \times \mathbf{x}_s$ and $\mathbf{l}_{js} = \mathbf{j} \times \mathbf{x}_s$ meeting at any point $\mathbf{x}_s \in \mathbf{l}_s$ different from $\mathbf{v}_s = \mathbf{l}_s \times \mathbf{l}_\infty$.

If the vanishing point $\mathbf{v}_\perp \in \mathbf{l}_s$ of the direction parallel to the SOR symmetry axis is known, the independent constraint $\mathbf{v}_s^T \omega \mathbf{v}_\perp = 0$ can be added to the system of (7), thus fixing one of the two degrees of freedom left for $\tilde{\omega}$. A parametrization for these ∞^1 conics is then

$$\tilde{\omega}(r) = r \mathbf{l}_\infty \mathbf{l}_\infty^T + (\mathbf{l}_{i\perp} \mathbf{l}_{j\perp}^T + \mathbf{l}_{j\perp} \mathbf{l}_{i\perp}^T), \quad (23)$$

where $\mathbf{l}_{i\perp} = \mathbf{i} \times \mathbf{v}_\perp$ and $\mathbf{l}_{j\perp} = \mathbf{j} \times \mathbf{v}_\perp$. This last result is in accordance with the fact, discussed in [27], that the self-calibration equations involving the imaged circular points \mathbf{i} and \mathbf{j} bring only one independent constraint if the line $\mathbf{i} \times \mathbf{j}$ goes through any of the points of a self-polar triangle for ω —which, in our case, is $\mathbf{v}_\infty, \mathbf{v}_s, \mathbf{v}_\perp$.

APPENDIX C

SAMPLING METRICALLY AN IMAGED SOR PARALLEL

In this appendix, we derive a closed form solution to the general problem of finding the vanishing point \mathbf{v}_θ of the line l_θ that intersects, in the world plane π , a reference line l_0 with a given Euclidean angle θ . The imaged circular points \mathbf{i} and \mathbf{j} of π are supposed to be known, together with the vanishing point \mathbf{v}_0 of l_0 . We then use this result to obtain the

intersection point $\mathbf{x}(\theta, z)$ between the image $\mathcal{C}(z)$ of the SOR parallel on π and the visible imaged meridian $\chi(\theta)$.

The basic relation between the angle θ and the vanishing point \mathbf{v}_θ is provided by the Laguerre's formula [13]

$$\theta = \frac{1}{2i} \log(\{\mathbf{v}_\theta, \mathbf{v}_0, \mathbf{i}, \mathbf{j}\}), \quad (24)$$

where $\{\}$ denotes the usual cross ratio of four points. By expressing the generic point on the vanishing line \mathbf{l}_∞ of π as

$$\mathbf{v}(\lambda) = \mathbf{i} + \lambda(\mathbf{i} - \mathbf{j}), \quad (25)$$

(24) can be rewritten as

$$e^{i2\theta} = \{\lambda_\theta, \lambda_0, \lambda_i, \lambda_j\}, \quad (26)$$

where $\lambda_\theta, \lambda_0, \lambda_i$ and λ_j are the values of the complex parameter λ , respectively, for the points $\mathbf{v}_\theta, \mathbf{v}_0, \mathbf{i}$ and \mathbf{j} . In particular, it holds $\lambda_i = 0$ and $\lambda_j = -1$; the values λ_θ and λ_0 are derived hereafter.

Taken any image line $\mathbf{l}_0 = (l_1, l_2, l_3)$ through \mathbf{v}_0 and distinct from \mathbf{l}_∞ and set $\mathbf{i} = \text{conj}(\mathbf{j}) = (a + ib, c + id, 1)$, solving for λ_0 the equation $\mathbf{l}_0^T \mathbf{v}(\lambda_0) = 0$, we get $\lambda_0 = -\frac{1}{2} [1 + i \tan \phi_0]$, where the angle

$$\phi_0 = \arctan\left(-\frac{l_1 a + l_2 c + l_3}{l_1 b + l_2 d}\right) \quad (27)$$

embeds in a compact way all the information about the reference line \mathbf{l}_0 and the circular points.

Substituting the above value of λ_0 into (26), the value of λ_θ can be computed as

$$\lambda_\theta = -\frac{1}{2} [1 + i \tan(\phi_0 + \theta)], \quad (28)$$

which eventually yields the required vanishing point as $\mathbf{v}_\theta = \mathbf{i} + \lambda_\theta(\mathbf{i} - \mathbf{j})$. In the particular case of an SOR image, the vanishing point \mathbf{v}_θ can be computed as above with the point $\mathbf{v}_s = \mathbf{l}_s \times \mathbf{l}_\infty$ and the image line \mathbf{l}_s as the reference \mathbf{v}_0 and \mathbf{l}_0 , respectively, (see Fig. 8b). The image line $\mathbf{l}_\theta = \mathbf{v}_\theta \times \mathbf{o}$, where $\mathbf{o} = \mathcal{C}^{-1}(z)\mathbf{l}_\infty$ is the image of the parallel's center, intercepts the imaged parallel \mathcal{C} at two points, of which the required point $\mathbf{x}(\theta, z)$ on the visible imaged meridian $\chi(\theta)$ is the farthest one from \mathbf{v}_θ along the line \mathbf{l}_θ .

ACKNOWLEDGMENTS

This work was partially funded by the Italian Ministry for Education, University and Research (MIUR) in the context of the national project "LIMA3D—Low Cost 3D Imaging and Modelling Automatic System," 2003-2005. The authors would like to thank Dario Comanducci for his support in the preparation of the experiments.

REFERENCES

[1] S.M. Abdallah, "Object Recognition via Invariance," PhD thesis, The Univ. of Sydney, Australia, 2000.
 [2] S.M. Abdallah and A. Zisserman, "Grouping and Recognition of Straight Homogeneous Generalized Cylinders," *Proc. Asian Conf. Computer Vision*, pp. 850-857, 2000.
 [3] M. Armstrong, "Self-Calibration from Image Sequences," PhD thesis, Univ. of Oxford, England, 1996.
 [4] S. Boughnoux, "From Projective to Euclidean Space under any Practical Situation—A Criticism of Self-Calibration," *Proc. Int'l Conf. Computer Vision*, pp. 790-796, 1998.
 [5] M.P. do Carmo, *Differential Geometry of Curves and Surfaces*. Prentice-Hall, 1976.

[6] P. Cignoni, C. Rocchini, C. Montani, and R. Scopigno, "Multiple Textures Stitching and Blending on 3D Objects," *Proc. Eurographics Workshop Rendering*, pp. 127-138, 1999.
 [7] C. Colombo, D. Comanducci, A. Del Bimbo, and F. Pernici, "Accurate Automatic Localization of Surfaces of Revolution for Self-Calibration and Metric Reconstruction," *Proc. IEEE Workshop Perceptual Organization in Computer Vision*, 2004, (on CD-ROM).
 [8] C. Colombo, A. Del Bimbo, and F. Pernici, "Uncalibrated 3D Metric Reconstruction and Flattened Texture Acquisition from a Single View of a Surface of Revolution," *Proc. First Int'l Symp. 3D Data Processing, Visualization, and Transmission*, pp. 277-284, 2002.
 [9] G. Cross and A. Zisserman, "Surface Reconstruction from Multiple Views Using Apparent Contours and Surface Texture," *Proc. NATO Advanced Research Workshop Confluence of Computer Vision and Computer Graphics*, A. Leonardis, F. Solina, and R. Bajcsy, eds., pp. 25-47, 2000.
 [10] P.E. Debevec, C.J. Taylor, and J. Malik, "Modeling and Rendering Architecture from Photographs: A Hybrid Geometry and Image Based Approach," *Proc. ACM SIGGRAPH*, pp. 11-20, 1996.
 [11] D.W. Eggert and K.W. Bowyer, "Computing the Perspective Projection Aspect Graph of Solids of Revolution," *IEEE Trans. Pattern Analysis and Machine Intelligence*, vol. 15, no. 2, pp. 109-128, Feb. 1993.
 [12] O.D. Faugeras and R. Keriven, "Variational-Principles, Surface Evolution, PDEs, Level Set Methods, and the Stereo Problem," *IEEE Trans. Image Processing*, vol. 7, no. 3, pp. 336-344, 1998.
 [13] O.D. Faugeras and Q.-T. Luong, *The Geometry of Multiple Images*. MIT Press, 2001.
 [14] L.H. de Figueiredo, "Adaptive Sampling of Parametric Curves," *Graphics Gems V*, A. Paeth, ed., pp. 173-178, Academic Press, 1995.
 [15] A.W. Fitzgibbon, G. Cross, and A. Zisserman, "Automatic 3D Model Construction for Turn-Table Sequences," *3D Structure from Multiple Images of Large-Scale Environments*, R. Koch and L. Van Gool, eds. pp. 155-170, Springer-Verlag, 1998.
 [16] D.A. Forsyth, J.L. Mundy, A. Zisserman, and C.A. Rothwell, "Recognising Rotationally Symmetric Surfaces from Their Outlines," *Proc. European Conf. Computer Vision*, 1992.
 [17] A.D. Gross and T.E. Boult, "Recovery of SHGCs from a Single Intensity View," *IEEE Trans. Pattern Analysis and Machine Intelligence*, vol. 18, no. 2, pp. 161-180, Feb. 1996.
 [18] R.I. Hartley and R. Kaucic, "Sensitivity of Calibration to Principal Point Position," *Proc. European Conf. Computer Vision*, pp. 433-466, 2002.
 [19] R.I. Hartley and A. Zisserman, *Multiple View Geometry in Computer Vision*. Cambridge Univ. Press, 2000.
 [20] E. Hayman, L. de Agapito, and I. Reid, "Self-Calibration of Rotating and Zooming Cameras," Technical Report OUEL 0225/00, Dept. of Eng. Science, Univ. of Oxford, 2000.
 [21] P. Heckbert, "Fundamentals of Texture Mapping and Image Warping," MS thesis, CS Division, Univ. of California, Berkeley, 1989.
 [22] W. Heidrich, H. Lensch, and H.-P. Seidel, "Automated Texture Registration and Stitching for Real World Models," *Proc. Pacific Graphics*, pp. 317-326, 2000.
 [23] G. Jiang, H.T. Tsui, L. Quan, and A. Zisserman, "Single Axis Geometry by Fitting Conics," *Proc. European Conf. Computer Vision*, pp. 537-550, 2002.
 [24] G. Jiang, H. Tsui, L. Quan, and A. Zisserman, "Geometry of Single Axis Motions Using Conic Fitting," *IEEE Trans. Pattern Analysis and Machine Intelligence*, vol. 25, no. 10, pp. 1343-1348, Oct. 2003.
 [25] J.J. Koenderink, "What Does The Occluding Contour Tell Us About Solid Shape?" *Perception*, vol. 13, pp. 321-330, 1984.
 [26] J. LaVest, R. Glachet, M. Dhome, and J.T. LaPrestre, "Modeling Solids Of Revolution By Monocular Vision," *Proc. Int'l Conf. Computer Vision and Pattern Recognition*, pp. 690-691, 1991.
 [27] D. Liebowitz, "Camera Calibration and Reconstruction of Geometry from Images," PhD thesis, Univ. of Oxford, U.K., 2001.
 [28] D. Liebowitz, A. Criminisi, and A. Zisserman, "Creating Architectural Models from Images," *Proc. EuroGraphics*, pp. 39-50, 1999.
 [29] D. Liebowitz and A. Zisserman, "Metric Rectification for Perspective Images of Planes," *Proc. IEEE Conf. Computer Vision and Pattern Recognition*, pp. 482-488, 1998.
 [30] J. Liu, J. Mundy, D. Forsyth, A. Zisserman, and C. Rothwell, "Efficient Recognition of Rotationally Symmetric Surfaces and Straight Homogeneous Generalized Cylinders," *Proc. IEEE Conf. Computer Vision and Pattern Recognition*, 1993.

- [31] P.R.S. Mendonça, K.-Y.K. Wong, and R. Cipolla, "Epipolar Geometry from Profiles under Circular Motion," *IEEE Trans. Pattern Analysis and Machine Intelligence*, vol. 23, no. 6, pp. 604-616, June 2001.
- [32] J. Mundy and A. Zisserman, "Repeated Structures: Image Correspondence Constraints and Ambiguity of 3D Reconstruction," *Applications of Invariance in Computer Vision*, J. Mundy, A. Zisserman, and D. Forsyth, eds., pp. 89-106, Springer-Verlag, 1994.
- [33] P.J. Neugebauer and G. Klein, "Texturing 3D Models of Real World Objects from Multiple Unregistered Photographic Views," *Computer Graphics Forum*, vol. 3, no. 18, pp. 245-256, 1999.
- [34] I. Pitas, J.-M. Chassery, W. Puech, and A.G. Bors, "Projection Distortion Analysis for Flattened Image Mosaicing from Straight Uniform Generalized Cylinders," *Pattern Recognition*, vol. 34, no. 8, pp. 1657-1670, 2001.
- [35] M. Pollefeys, "Self-Calibration and Metric 3D Reconstruction from Uncalibrated Image Sequences," PhD thesis, K.U. Leuven, 1999.
- [36] J. Ponce, D. Chelberg, and W.B. Mann, "Invariant Properties of Straight Homogeneous Generalized Cylinders and Their Contours," *IEEE Trans. Pattern Analysis and Machine Intelligence*, vol. 11, no. 9, pp. 951-966, Sept. 1989.
- [37] A. Rappoport, M. Werman, E. Ofek, and E. Shilat, "Multi-resolution Textures from Image Sequences," *IEEE Computer Graphics and Applications*, vol. 17, no. 2, pp. 18-29, 1997.
- [38] M. Richetin, M. Dhome, J.T. Lapreste, and G. Rives, "Inverse Perspective Transform Using Zero-Curvature Contour Points: Application to the Localization of Some Generalized Cylinders from a Single View," *IEEE Trans. Pattern Analysis and Machine Intelligence*, vol. 13, no. 2, pp. 185-192, Feb. 1991.
- [39] H. Sato and T.O. Binford, "Finding and Recovering SHGC Objects in an Edge Image," *Computer Vision, Graphics, and Image Processing: Image Understanding*, vol. 57, pp. 346-358, 1993.
- [40] D. Scharstein and R. Szeliski, "A Taxonomy and Evaluation of Dense Two-Frame Stereo Correspondence Algorithms," *Int'l J. Computer Vision*, vol. 47, no. 1/2/3, pp. 7-42, 2002.
- [41] T. Sederberg and J. Zheng, "Algebraic Methods for Computer Aided Geometric Design," *Handbook of Computer Aided Geometric Design*, 2001.
- [42] S.M. Seitz and C.R. Dyer, "Photorealistic Scene Reconstruction by Voxel Coloring," *Proc. Image Understanding Workshop*, pp. 935-942, 1997.
- [43] J. Semple and G. Kneebone, *Algebraic Projective Geometry*. Oxford Univ. Press, 1952.
- [44] G. Slabaugh, W.B. Culbertson, T. Malzbender, and R. Schafer, "A Survey of Volumetric Scene Reconstruction Methods from Photographs," *Proc. Joint IEEE TCVG and Eurographics Workshop*, pp. 81-100, 2001.
- [45] P. Sturm and S.J. Maybank, "On Plane-Based Camera Calibration: A General Algorithm, Singularities, Applications," *Proc. Int'l Conf. Computer Vision and Pattern Recognition*, pp. 432-437, 1999.
- [46] P. Sturm and S.J. Maybank, "A Method for Interactive 3D Reconstruction of Piecewise Planar Objects from Single Images," *Proc. British Machine Vision Conf.*, pp. 265-274, 1999.
- [47] R. Szeliski, "Rapid Octree Construction from Image Sequences," *Computer Vision, Graphics, and Image Processing*, vol. 58, no. 1, pp. 23-32, 1993.
- [48] F. Ulupinar and R. Nevatia, "Shape from Contour," *IEEE Trans. Pattern Analysis and Machine Intelligence*, vol. 17, no. 2, pp. 120-135, Feb. 1995.
- [49] S. Utcke and A. Zisserman, "Projective Reconstruction of Surfaces of Revolution," *Proc. DAGM-Symp. Mustererkennung*, pp. 265-272, 2003.
- [50] L. Van Gool, M. Proesmans, and A. Zisserman, "Planar Homologies as a Basis for Grouping and Recognition," *Image and Vision Computing*, vol. 16, pp. 21-26, 1998.
- [51] K.-Y.K. Wong, "Structure and Motion from Silhouettes," PhD thesis, Univ. of Cambridge, U.K., 2001.
- [52] K.-Y.K. Wong and R. Cipolla, "Structure and Motion from Silhouettes," *Proc. Eighth IEEE Int'l Conf. Computer Vision*, pp. 217-222, 2001.
- [53] K.-Y.K. Wong, P.R.S. Mendonça, and R. Cipolla, "Camera Calibration from Symmetry," *Proc. Ninth IMA Conf. Math. of Surfaces*, R. Cipolla and R. Martin, eds., pp. 214-226, 2000.
- [54] K.-Y.K. Wong, P.R.S. Mendonça, and R. Cipolla, "Reconstruction of Surfaces Of Revolution from Single Uncalibrated Views," *Proc. British Machine Vision Conf.*, P.L. Rosin and D. Marshall, eds., pp. 93-102, 2002.

- [55] K.-Y.K. Wong, P.R.S. Mendonça, and R. Cipolla, "Camera Calibration from Surfaces of Revolution," *IEEE Trans. Pattern Analysis and Machine Intelligence*, vol. 25, no. 2, pp. 147-161, Feb. 2003.
- [56] M. Zerroug and R. Nevatia, "Part-Based 3D Descriptions of Complex Objects from a Single Image," *IEEE Trans. Pattern Analysis and Machine Intelligence*, vol. 21, no. 9, pp. 835-848, Aug. 1999.
- [57] A. Zisserman, J. Mundy, D. Forsyth, J. Liu, N. Pillow, C. Rothwell, and S. Utcke, "Class-Based Grouping in Perspective Images," *Proc. Int'l Conf. Computer Vision*, pp. 183-188, 1995.



Carlo Colombo received the MS degree cum laude in electronic engineering (1992) from the University of Florence, Italy, and the PhD degree in robotics (1996) from the Sant'Anna School of University Studies and Doctoral Research, Pisa, Italy. He currently is an associate professor at the Department of Systems and Informatics of the University of Florence, where he teaches courses on computer architectures and computer vision. From 1996 to 1999, he was an assistant professor at the Department of Electronics for Automation, University of Brescia, Italy. His main research interests include computer vision and its applications to human-computer interaction, advanced robotics and multimedia systems. From 1996 to 2000, he was the secretary of the Italian Chapter of the International Association for Pattern Recognition (IAPR). Professor Colombo presently is an editorial board member of the international journal *Robotics and Autonomous Systems* and serves on the program committee of several international conferences in the area of visual information processing.



Alberto Del Bimbo is full professor of computer engineering at the University of Florence, Italy. From 1997 to 2000, he was the Director of the Department of Systems and Informatics at the University of Florence. From 1998 to the present, he was the Director of the Master in Multimedia, and from 2000 to present is the Deputy Rector of the University of Florence, in charge of Research and Innovation Transfer. His scientific interests are pattern recognition, image databases, and multimedia. He has delved into object recognition and image sequence analysis, image and video database content based retrieval, and advanced man-machine interaction. Professor Del Bimbo is the author of more than 180 publications that have appeared in the most distinguished international journals and conference proceedings. He is the author of the monograph *Visual Information Retrieval* on content-based retrieval from image and video databases. He has also been the guest editor of many special issues on image databases in many highly respected journals. Professor Del Bimbo was the general chairman of the Ninth IAPR International Conference Image Analysis and Processing, ICIAP '97, Florence 1997, and of the Sixth IEEE International Conference Multimedia Computing and Systems, ICMCS '99, Florence 1999. He was the president of IAPR from 1996 to 2000, Member-at-Large of IEEE Pubs Board from 1999 to 2001, and was appointed Fellow of IAPR the International Association for Pattern Recognition, in 2000. Professor Del Bimbo is presently an associate editor of *Pattern Recognition*, *Journal of Visual Languages and Computing*, *Multimedia Tools and Applications Journal*, *Pattern Analysis and Applications*, *IEEE Transactions on Multimedia*, and *IEEE Transactions on Pattern Analysis and Machine Intelligence*.



Federico Pernici received the MS degree in computer engineering from the University of Florence, Italy, in 2002, and he is currently pursuing the PhD degree on informatics and telecommunications at the University of Florence. His research interests are computer vision, pattern recognition, and computer graphics.